Monthly Notices of the ROYAL ASTRONOMICAL SOCIETY

MNRAS **526,** 1112–1121 (2023) https://doi.org/10.1093/mnras/stad2779
Advance Access publication 2023 September 12

# Detection of optical emission from the supernova remnant G7.7–3.7†

V. Domček [1,2★] J. V. Hernández Santisteban [3] A. Chiotellis [4,5] P. Boumis [4] J. Vink [1,2,6] S. Akras [4] D. Souropanis [4,7,8] P. Zhou [1,9] and A. de Burgos [8,10,11]

[1]*Anton Pannekoek Institute for Astronomy, University of Amsterdam, Science Park 904, NL-1098 XH Amsterdam, the Netherlands*
[2]*GRAPPA, University of Amsterdam, Science Park 904, NL-1098 XH Amsterdam, the Netherlands*
[3]*SUPA Physics and Astronomy, University of St Andrews, KY16 9SS St. Andrews, UK*
[4]*Institute for Astronomy, Astrophysics, Space Applications and Remote Sensing, National Observatory of Athens, 15236 Penteli, Greece*
[5]*4th Lykeion Acharnon, Ag. Petrou and Echinou, 13674 Acharnes, Greece*
[6]*SRON, Netherlands Institute for Space Research, Niels Bohrweg 4, 2333 CA, Leiden, the Netherlands*
[7]*Department of Physics, National and Kapodistrian University of Athens, Panepistimiopolis, 15784 Zografos, Greece*
[8]*Isaac Newton Group of Telescopes, Apartado 321, E-38700 Santa Cruz de La Palma, Canary Islands, Spain*
[9]*School of Astronomy and Space Science, Nanjing University, Nanjing 210023, People's Republic of China*
[10]*Dpto. Astrofísica, Universidad de La Laguna, E-38206 La Laguna, Tenerife, Spain*
[11]*Instituto de Astrofísica de Canarias, Avenida Vía Láctea, E-38205 La Laguna, Tenerife, Spain*

Accepted 2023 September 4. Received 2023 September 4; in original form 2022 December 7

## ABSTRACT

We present the first optical study of the supernova remnant (SNR) G7.7–3.7, with the aim of determining its evolutionary phase since it has been suggested to be the remnant of SN 386 AD. We obtained narrow-band images in the filters H $\alpha$ + [N II], H $\beta$, [O III], [S II] that revealed faint optical emission in the southern region of the SNR consisting of two filaments elongated in the east–west direction aligned with the X-ray emitting region of the remnant. The filaments were seen in H $\alpha$ + [N II], [O III] images and marginally in the [S II] images, with a non-detection in H $\beta$. Long-slit spectroscopy of the three regions along one filament revealed large ratios of [S II]/H $\alpha$ = (1.6–2.5), consistent with that expected for a shock-heated SNR. The [S II] doublet ratio observed in two of the regions implies an upper limit for the electron density of the gas, with estimates falling below 400 cm$^{-3}$ and 600 cm$^{-3}$ in the respective areas. We discuss potential physical mechanisms that formed the observed optical filaments and we suggest that most likely they resulted by a collision of the SNR with a dense circumstellar shell lying at the southern region of the remnant.

**Key words:** shock waves – techniques: photometric – techniques: spectroscopic – supernovae: SN 386 – ISM: G7.7-3.7 – ISM: supernova remnants.

## 1 INTRODUCTION

Supernova remnants (SNRs) result from the interaction between an interstellar, or circumstellar, medium and a shock wave, initiated by energetic supernovae (SNe) that mark the death of massive stars or by the thermonuclear combustion of white dwarfs in interactive binaries. They are regarded as factories of cosmic rays in our Galaxy, the hosts of young neutron stars, and are essential for studies of astrophysical shocks (see Vink 2020, for a review). Optical emission, in particular, plays an essential role in the studies of SNRs as most of the extragalactic SNRs have been identified and characterized only using optical observations (Leonidaki, Boumis & Zezas 2013; Long 2017). The optical band plays a less dominant but still an important role in the study of Galactic SNRs. It provides vital constraints on the ambient-medium densities and shock speeds of two distinct regimes of astrophysical shocks – radiative and non-radiative.

Radiative shocks exist in regions of SNRs where the shock has significantly slowed down ($\lesssim$200 km s$^{-1}$). In the optical range, this leads to the formation of prominent H $\alpha$, [S II], [O III], and also [N II] emission lines. Due to the necessity of low shock velocities, radiative shocks are mostly associated with evolved SNRs, such as N49 (Bilikova et al. 2007) or HB3 (Boumis et al. 2022), but are not exclusive to them. Younger SNRs like Kepler (see Vink 2016, for a review), Cas A (Milisavljevic & Fesen 2013), and even SN 1987A (Mccray 2016) also exhibit radiative optical emission originating in dense clumps of circumstellar material (often rich in nitrogen) or ejecta (rich in carbon-burning products or intermediate-mass elements), where the shock has locally slowed down due to the presence of higher density gas.

Non-radiative shocks are formed when the cooling time-scale of the shocked gas is substantially larger than the dynamical time-scale of the forward shock expansion. These are found in SNRs that are characterized by relatively high velocities ($\gtrsim$200 km s$^{-1}$) propagating in a moderately low density environment. Consequently,

★ E-mail: vdomcek@gmail.com

† Based on observations made with the Isaac Newton Telescope operated on the island of La Palma by the Isaac Newton Group of Telescopesin the Spanish Observatorio del Roque de los Muchachos of the Instituto de Astrof´ısica de Canarias

non-radiative shocks are found in young (e.g. Tycho's SNR; Ghavamian et al. 2000) or in evolved SNRs that have maintained their high speed due to their propagation in a low-density ambient medium (e.g. Cygnus Loop; Hester, Raymond & Blair 1994). Non-radiative shocks are often accompanied by pure Balmer-line emission from the SNR shock fronts, seen pre-dominantly in the early phases of the SNR evolution and are almost exclusively present in young Type Ia SNRs (e.g. SN1006, SNR 0509-67.5). The emission is observed in very thin filaments originating in regions with higher shock speeds (Heng 2010) which are thought to be important sites for cosmic-ray acceleration (Chevalier, Raymond & Kirshner 1980; Vink et al. 2010; Morlino et al. 2013; Vink & Yamazaki 2013).

Historical SNRs – e.g. SN1006, Tycho, and Kepler – form only a small fraction of the SNR population and have been well studied at optical wavelengths. Recently, Zhou et al. (2018) suggested that G7.7–3.7 (PKS 1814-24) belongs to this category, being the potential SNR of SN 386 AD. Moreover, G7.7–3.7 might be one of a few known historical SNRs that resulted from a very low luminosity SN and, therefore, could be of particular value for studying the evolution and origin of this small group of SNe (< 5 per cent of all Type II SNe; Pastorello et al. 2004). Recent studies found that SN 1181 was also a subluminous Type Iax historical SN (Schaefer 2023), and its probable remnant is a newly identified nebula called Pa 30 (Ritter et al. 2021).

G7.7–3.7 has not been extensively studied in the past, but the suggestion that G7.7–3.7 may be the remnant of a low- luminosity historical SN heightens the need to study this SNR more closely. G7.7–3.7 was first listed as a radio source with a linear polarization of $\sim$ 10 per cent in early catalogues from 1960s (Gardner, Whiteoak & Morris 1969). The high degree of polarization was an early indication that G7.7–3.7 is an SNR. Subsequent targeted radio investigations (Milne & Dickel 1974; Milne et al. 1986; Dubner et al. 1996) revealed an extended object with a shell-like structure, with angular diameter of $\sim$22 arcmin and the overall radio spectral index $\alpha \sim 0.32$, flatter than the average index for SNRs (see Vink 2020, fig. 12.2). The distance has been suggested to be $4.5 \pm 1.5$ kpc based on the $\Sigma$–D (surface brightness–diameter) relation (Milne et al. 1986; Pavlovic et al. 2014; Green 2015). The visual extinction as measured from X-ray data was found to be relatively low, $A_{\rm v} \sim 1.2 \pm 0.2$ (Zhou et al. 2018).

So far, investigations of G7.7–3.7 in the optical (van den Bergh 1978) or $\gamma$-rays (Acero et al. 2016) did not yield the detection of an SNR. In mid-infrared, three dust regions with temperatures of 50–100 K were identified (Milne et al. 1986; Arendt 1989). The brightest one is centred on a planetary nebula in the field-of-view of the SNR, the second is coincident with the location of radio bright and steep feature ($\alpha \sim -0.6$) in the west of the SNR, and the third lies just outside of the radio shell in the south-east of G7.7–3.7 (Milne et al. 1986). Later studies in X-rays (Giacani et al. 2010; Zhou et al. 2018) have shown an X-ray counterpart to the radio structure in the south of the SNR, and a point-like source in the north-east (Giacani et al. 2010). An X-ray analysis of the southern shock region indicates the age of the plasma to be $t \sim 1.2 \pm 0.6$ kyr, based on the ionization age (Zhou et al. 2018), with largely subsolar abundances indicating a shocked interstellar medium.

In this work, we report on deep targeted optical observations of SNR G7.7–3.7. In particular, we obtained images using narrow-band filters covering the emission lines of H$\alpha$ + [N II], H$\beta$, [O III], [S II] and low-resolution spectra covering the range of 3500–9800 Å. In Section 2, we describe the data reduction process, while in Section 3, we report on our findings and discuss potential implications for the SN 386 AD origin scenario.

## 2 OBSERVATIONS AND ANALYSIS

### 2.1 Imaging

We observed SNR G7.7–3.7 on 2019 August 22–25 (program ID:ING.NL.19B.006) and on 2022 June 23. The observations were performed using the Wide Field Camera (WFC) instrument, at the prime focus of the 2.5m Isaac Newton Telescope (INT), in La Palma, Spain. The field-of-view of the detector is $\sim$34 arcmin $\times$ 34 arcmin with a pixel scale of 0.333 arcsec pix$^{-1}$. In 2019, we obtained data in the narrow-band filters H$\alpha$ + [N II], H$\beta$, [O III], [S II] and the SDSS broad-band filters $r'$, $g'$, which were used for continuum subtraction. In 2022, we expanded the data set with additional observations with the H$\beta$ and $g'$ filters. The observations were performed in a dither pattern to fill the gaps between its four chips. Sky flat fields were taken nightly during the morning and evening twilight.

The 2019 data were pre-selected based on the average full width at half-maximum and the number of stars detected in each image (see Table 1 for details on image quality per filter). Several additional images had to be excluded due to unexplained anomalous behaviour of the detector. This resulted in combined exposure times in the narrow-band filters H$\alpha$ + [N II], H$\beta$, [O III], [S II] of 90, 15, 37, 30 min respectively, and two broad-band filters, $r'$ and $g'$, with exposures times of 5 min.

Data reduction of the 2019 data was performed with the THELI (v2) software (Erben et al. 2005; Schirmer 2013), using the default settings with exceptions in background modelling.[1] We used the option of `smoothing scale for background model` with a set value of 300px and changed the co-addition setting to the median. We used the Gaia DR1 catalogue (Gaia Collaboration 2016a, b) within THELI with a magnitude limit of 18 mag in order to improve our astrometric solution of the field. We did not use the THELI sky-background subtraction option at this stage. For further analysis, we reprojected all images to a common world coordinate system using the H$\alpha$ + [N II] image as a reference. We employ `reproject_interp` of the ASTROPY affiliated library REPROJECT, which aligns and reprojects data to a new common pixel grid using interpolation in order to match physical pixel coordinates between the images (Astropy Collaboration 2013). Based on the examination of the THELI-produced count-rate mosaic images, a minor systematic background correction was deemed necessary to bring the background levels closer to zero. The correction values for individual filters are shown in Table. 1.

The 2022 narrow-band H$\beta$ and broad-band $g'$ images were processed separately using a newer version of THELI (v3). We followed the same procedure as for the 2019 data set with the exception of using a newer Gaia DR3 catalogue[2] (Gaia Collaboration 2022). Resulting combined exposure time is 125 min in the narrow-band H$\beta$ filter and 20 min in the broad-band $g'$ filter.

#### 2.1.1 *Flux calibration and continuum subtraction*

We performed a flux calibration to obtain the continuum subtracted images. We used Pan-STARRS DR2 (Flewelling et al. 2020) as a calibration catalogue, with stars selected from the 5 arcsec cone

[1]Recommended setting of the `focal plane array handling` parameters were for *Gaia* DR1 and WFC detector in THELI (v2) following:
Stability type - instrument; Mosaic type - same crval; FPA mode - new
[2]Recommended setting of the `focal plane array handling` parameters were for *Gaia* DR3 and WFC detector in THELI (v3) following:
Stability type - exposure; Mosaic type - loose; FPA mode - ignore prior

**Table 1.** Summary of the broad- and narrow-band filters used in this study. The central wavelength, λ, and the effective width, Δλ, are shown for each filter. We provide information on the average observing conditions and parameters used in the absolute flux calibration of each co-added image.

| Obs. year | Filter name | Filter λ [Å] | Filter Δλ [Å] | Average seeing [arcsec] | Average air mass | Total exp. time [min] | Systematic bkg. correction [ct $s^{-1}$] | Zero point calibration |
|---|---|---|---|---|---|---|---|---|
| 2019 | Sloan $r'$ | 6240 | 1347 | 1.1 | 1.7 | 5 | 1.00 | $24.846 \pm 0.004$ |
| | Sloan $g'$ | 4846 | 1285 | 2.0 | 2.5 | 5 | 0.46 | $24.644 \pm 0.008$ |
| | H $\alpha$ + [N II] | 6568 | 95 | 1.2 | 1.7 | 90 | 0.10 | $21.880 \pm 0.005$ |
| | H $\beta$ | 4861 | 30 | 2.0 | 1.8 | 15 | 0.014 | $20.705 \pm 0.017$ |
| | [O III] | 5008 | 100 | 1.9 | 2.2 | 37 | 0.06 | $22.097 \pm 0.014$ |
| | [S II] | 6725 | 80 | 2.0 | 2.0 | 30 | 0.14 | $21.840 \pm 0.011$ |
| 2022 | Sloan $g'$ | 4846 | 1285 | 1.6 | 1.6 | 20 | 0.5 | $26.403 \pm 0.007$ |
| | H $\beta$ | 4861 | 30 | 1.7 | 1.6 | 125 | −0.02 | $22.115 \pm 0.015$ |

centred at the selected shock region (indicated by the rectangle region in Fig. 1). Pan-STARRS catalogue brightness range was limited to 13–17 mag in order to avoid star saturation on the brighter end and source confusion on the fainter end. The one exception concerns the $g'$ filter data obtained in 2022. Here the range was expanded to 21 mag due to the longer exposure causing saturation of stars in the lower range.

The source catalogue of the observed INT data was constructed using the SExtractor (Bertin & Arnouts 1996). We limited the use of the source catalogue only to stars with a clear detection, represented by the FLAG = 0 condition. An airmass correction was performed using the average airmass value per filter listed in Table 1. We cross-matched the two catalogues with the distance precision of 1 arcsec between two given stars. In the case of the broad-band filters, both Pan-STARRS and WFC use identical *r-SDSS* and *g-SDSS* filters, and after the airmass correction, both catalogues can be directly compared. However, since there are no directly comparable narrow-band filter fluxes, we performed an additional step to calculate them from the available broad-band filter values.

First, we employed the broad-band photometry of Pan-STARRS to retrieve the effective temperature of selected stars based on the Castelli & Kurucz (2003) stellar atmosphere models (3500–50 000 K). We then found the best temperature model $M(T_{\rm eff})$ and scaling $A$, for every star such that $F(\lambda, T_{\rm eff}) = A \cdot M(T_{\rm eff})$ using a simple linear interpolation over the grid. We only included stars with fitted temperatures above 3750 K, which we selected in order to avoid extrapolating outside the model grid boundary (3500 K). For every fitted star, we performed synthetic photometry in the wide- and narrow-band filters of the WFC images[3] to create a star catalogue.

We obtained the absolute calibration of the image by fitting the ensemble instrumental magnitudes in each filter to determine the global zero-point based on our synthetic model prediction using a linear regression model. We fitted for the zero-point value two times, applying a $3\sigma$-clipping procedure to remove outliers between the two iterations. We also excluded stars brighter than $m < 17$, to avoid saturation effects in $r'$ and $i'$ filters. The resulting zero-point values for each WFC filter, which are then applied to the count-rate images, are shown in Table 1.

Finally, to perform the continuum subtraction on the narrow-band images ($r'$ for H $\alpha$ + [N II] and [S II]; $g'$ for H $\beta$ and [O III]) we had to further smooth the images to match the point-spread functions (PSFs) to common values between images. We have used the source catalogue obtained by SExtractor to obtain a distribution of PSFs, and chose a smaller region with non-saturated stars in each image for comparison. We then used the *gaussian_filter* from the *scipy* library to achieve the best match of PSFs. The following $\sigma$ values for the Gaussian kernel for individual filters were applied: $\sigma = 0.54$ pix to smooth $r'$ filter for H $\alpha$ correction; $\sigma = 2.25$ pix to smooth $r'$ filter for [S II] correction; $\sigma = 1.39$ pix to smooth [O III] filter to match $g'$ filter. No smoothing was applied for the 2022 H $\beta$ and $g'$ filters.

After the reprojection, flux calibration, PSF matching, and a background adjustment, we were able to obtain the continuum-subtracted images by simple subtraction. We present the resulting images in our region of interest in Fig. 2.

### 2.2 Spectroscopy

Low-dispersion long-slit spectra were obtained with the 2.5m INT, on La Palma, Spain on 2022 July 4. Three spectra (1800 s, 900 s, 900 s) of Filament B were taken, resulting in a total exposure time of 3600 s. The R300V grating of the IDS spectrometer was used in conjunction with the Red + 2/EEV10 CCD (1 × 1 binning mode), resulting in a spatial scale of 0.44 arcsec $pixel^{-1}$ covering the range 3500–9800Å. The slit has a width of 1.″2 and a useful length of 3.′3 and it was oriented in the east–west direction. The coordinates of the position centres of each spectrum are given in Table 2. For the absolute flux calibration the spectrophotometric standard star SP1550 + 330 was used. The data reduction was performed using standard routines of the IRAF package (Tody 1986). All spectra were bias-subtracted and flat-field–corrected using a series of well-exposed twilight frames, while they were calibrated against the reference spectrum of a CuAr + CuNe arc lamp. The position of the slit as well as the spectra are shown in Figs 3 and 4, respectively.

## 3 RESULTS AND DISCUSSION

### 3.1 Detection of optical emission

Two faint filamentary structures are detected in H $\alpha$ + [N II], [O III], and marginally in [S II] narrow-band images, located in the southern part of the SNR (see Fig. 2). Similar structures also appear in the SuperCOSMOS H $\alpha$ imaging survey (Parker et al. 2005). For the purposes of this work, we name these two structures Filaments A and B, as labelled in Fig. 2. Aside from the southern section there is no obvious detection of a diffuse emission in other parts of the SNR.

Both filaments are elongated in the east–west direction. In particular, Filament A positioned at the forefront of the X-ray emission (associated to the X-ray forward shock, see lower left region in Fig. 2), emitting mainly in H $\alpha$ + [N II] and partially in [O III]. On the other hand, Filament B lies in the fainter location in X-rays (upper right in Fig. 2) and, although elongated in the east-west direction,

[3]Transmission curves for narrow-band filters were obtained from the WFC website at http://catserver.ing.iac.es/filter/list.php?instrument = WFC.

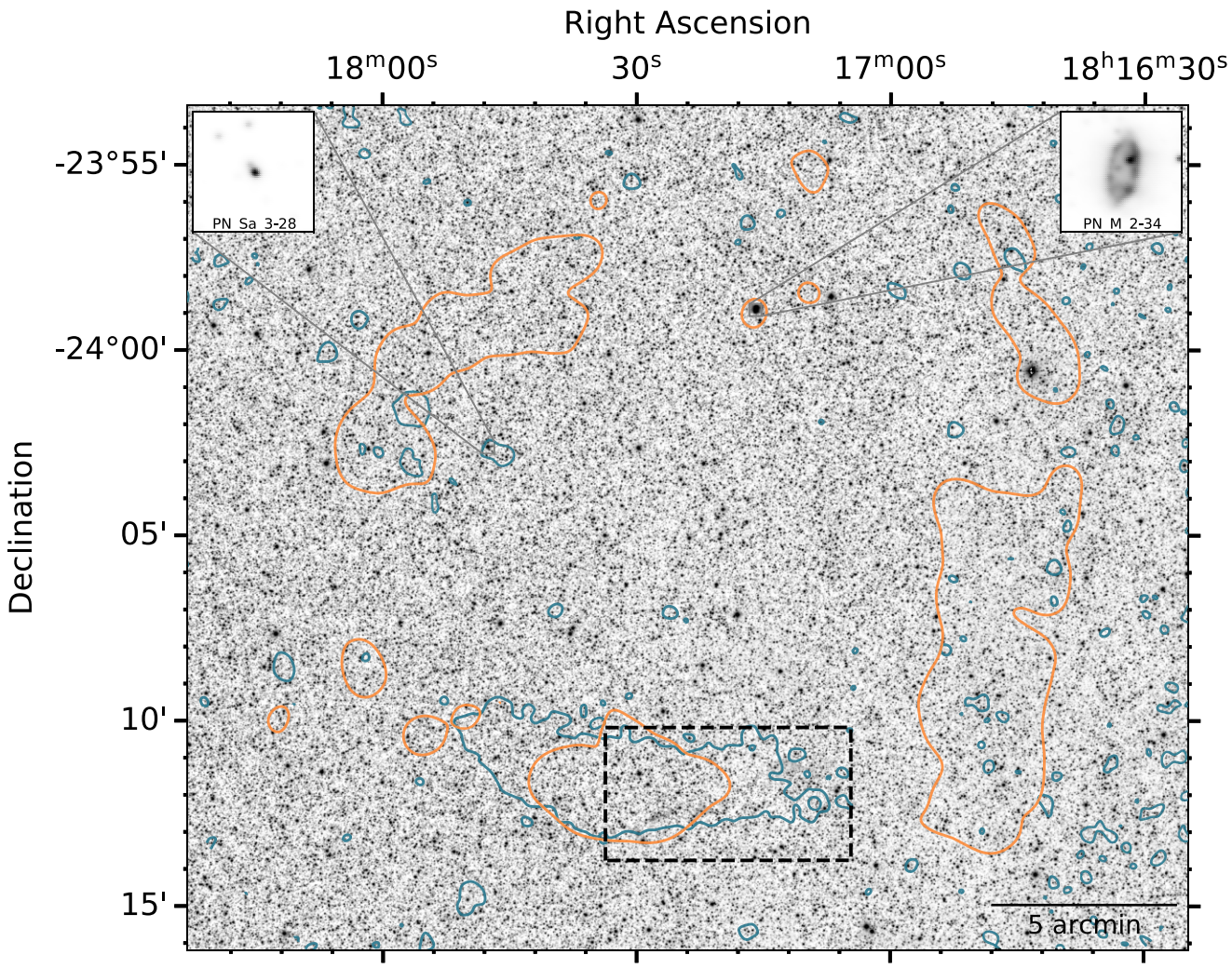


**Figure 1.** A mosaiced H $\alpha$ + [N II] count rate image of SNR G7.7–3.7. Orange colour displays 1.4 GHz NVSS radio (Kaplan et al. 1998) contours at flux level of 0.003 Jy beam$^{-1}$, while the blue colour represents *XMM–Newton* (0.5-5.0) keV contours at flux level of $7 \times 10^{-5}$ ct s$^{-1}$ (see fig. 1 in Zhou et al. (2018) for full view of radio and X-rays). Dashed rectangle displays a region with the detected optical emission, further used for analysis in Fig. 2. The field-of-view also contains two planetary nebulae (PN Sa 3-28 (Perek & Kohoutek 1967) and PN M 2-34 (Sanduleak 1976)) shown in the upper corners of the figure with different scaling and 10× magnification.

it has a more extended diffuse structure compared to Filament A. It is also visible in H $\alpha$ + [N II] and [O III], with a similar, but less significant structure in [S II]. The H $\beta$ image does not show any significant emission even with the extended 2 h exposure time.

### 3.2 Line ratio diagnostic of filaments

The ratio between [S II] doublet lines (at 6716 and 6731 Å) and H $\alpha$ is commonly used to determine the nature of excitation in the emission regions of SNR and planetary nebulae (PNe). In particular, shock-heated SNR exhibits an enhanced ratio of [S II]/H $\alpha$ $> 0.4$ (Long 2017), which is in contrast to the lower ratio typically observed in H II regions ([S II]/H $\alpha$ $\approx 0.1$) or PNe ([S II]/H $\alpha$ $< 0.4$). From our imaging alone it is not possible to distinguish the emission mechanism given that narrow-band filters contain several lines from different species (see Fig. 4), skewing the measurements and thus resulting in ambiguous inferences.

Thus, to determine the nature of the optical emission in G7.7–3.7, a low-resolution long-slit spectrum of Filament B was obtained. Three integrated spectra of Filament B were extracted with an aperture length of 20.2, 10.6, and 11.4 arcsec (for positions 1, 2, and 3, respectively) and their exact position is shown in Fig. 3. The extracted spectra are illustrated in Fig. 4 where the H $\alpha$, [N II] $\lambda\lambda$6548,6584 and [S II] $\lambda\lambda$6716,6731 emission lines are clearly detected. The observed lines fluxes, normalized to F(H $\alpha$) = 100, are listed in Table 3. The band-passes of the H $\alpha$ + [N II] and [S II] filters used for the imaging data of G7.7–3.7 are also overplotted for reference.

While Filament B is clearly detected in our [O III] image (see Fig. 2), our spectroscopic data do not show any [O III] nor H $\beta$ line emission (the latter consistent with our null detection in both epochs of deep H $\beta$ imaging). However, the slit position on Filament B can explain the missing [O III] emission lines. Fig. 3 shows the position of the slit (red line) across Filament B in the H $\alpha$ + [N II] (left) and [O III] (right) images. We can easily discern a spatial offset of ~2 arcsec between the two images. An offset between the [O III] and H $\alpha$ regions is expected to be found in SNRs and more generally in shocked gases (e.g. Boumis et al. 2022). Just behind the shock front, the gas is highly ionized and emission lines like [O III] are

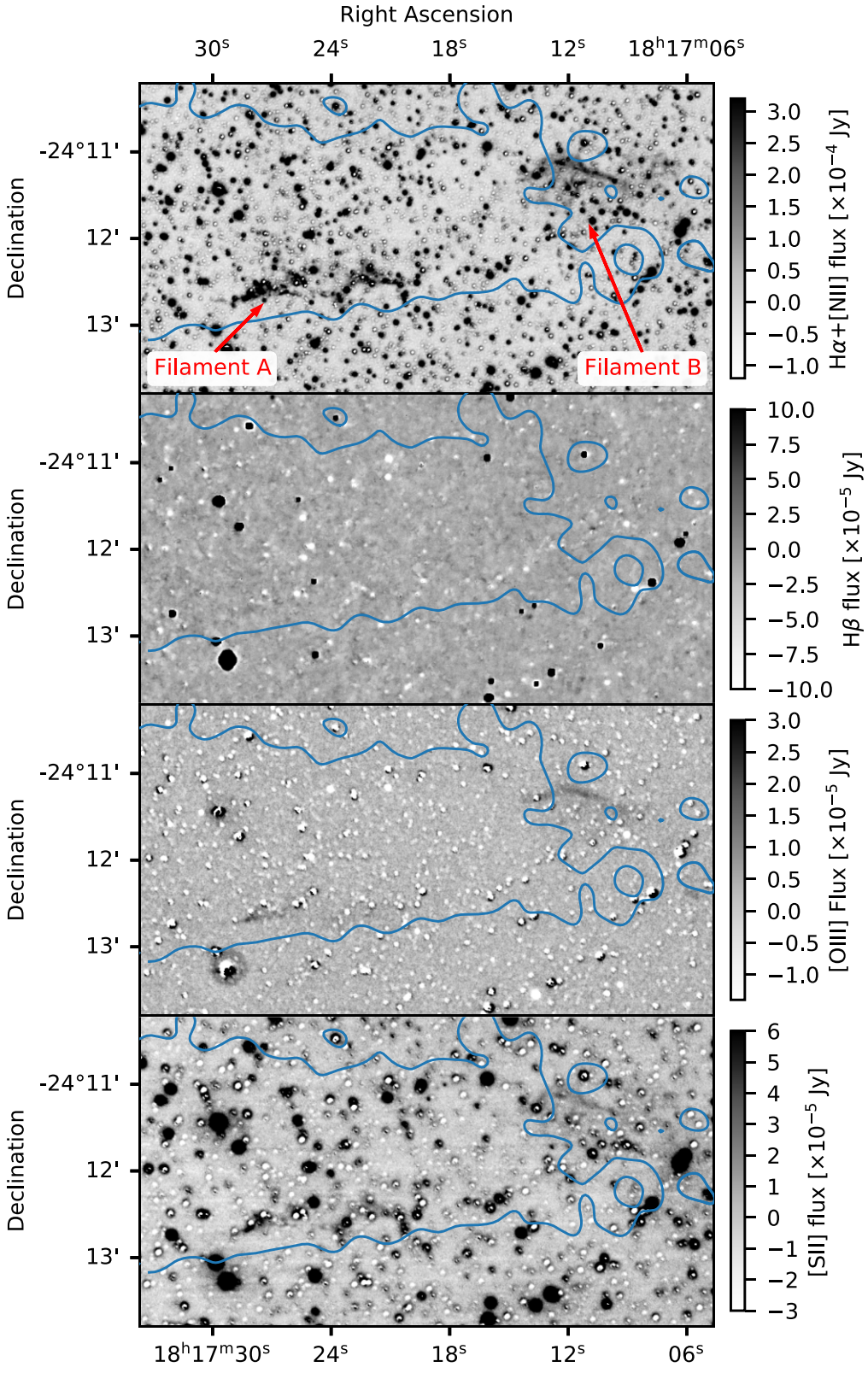


**Figure 2.** Continuum subtracted images in narrow-band filters from top to bottom – H $\alpha$ + [N II], H $\beta$, [O III], and [S II], displaying the two filaments detected. Contours are the same as in Fig. 1.

**Table 2.** Log of spectroscopic observations on Filament B. The total exposure time was divided in three individual exposures (see the text for details).

| | Position centre | | Exp. time | Length[a] |
|---|---|---|---|---|
| | $\alpha$ | $\delta$ | (s) | (arcsec) |
| Pos.1 | $18^h17^m12\overset{s}{.}7$ | -24°11′05″ | 3600 | 20.2 |
| Pos.2 | $18^h17^m11\overset{s}{.}6$ | -24°11′05″ | 3600 | 10.6 |
| Pos.3 | $18^h17^m07\overset{s}{.}5$ | -24°11′05″ | 3600 | 11.4 |

[a]Extraction aperture lengths for each position.

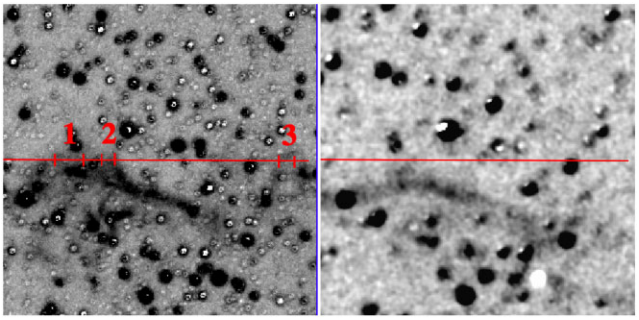


**Figure 3.** Slit position (red line) across Filament B region in the H $\alpha$ + [N II] (left) and [O III] (right) images. The apertures of positions 1, 2, and 3 are also shown (see Table 2). North is to the top, east to the left. We find an ∼2 arcsec offset between the H $\alpha$ + [N II] and [O III] filaments (see Section 3.2 for further discussion).

found. Subsequently, the gas cools down and recombines, resulting in H $\alpha$ emission further back from the shock front. This spatial offset between line-emitting regions is thus consistent with the filament moving away from the geometrical centre of the SNR.

In Fig. 5, we present the common H $\alpha$/[N II] versus H $\alpha$/[S II] line ratio diagnostic diagram to disentangle UV-dominated from shock-dominated structures (Sabbadin, Minello & Bianchini 1977; Akras et al. 2022). This diagram is populated with observed line ratios from a sample of SNRs and PNe together with the regions of parameter space occupied by SNRs, PNe and H II-regions. The line ratios of G7.7–3.7 measured in this work are presented with black circles and are well within the region of SNRs. The H $\alpha$/[S II] line ratio is found to be significantly smaller compared to UV-dominated regions, ranging from −0.4 up to −0.26 (in logarithmic scale). The low H $\alpha$/[S II] ratio obtained from Filament B is close to the ones found in another SNR, G39.7–7.2 (Boumis et al. 2007). According to our spectroscopic data and the analysis above, the SNR nature of the Filament B is verified. Based on the observed [S II] F(6716)/F(6731) ratios and utilizing equation 7 of Samarakoon (2018) we can estimate the electron density, $n_e$, of both regions. Assuming a characteristic electron temperature of $T_e = 10^4$ K (Samarakoon 2018), we estimated upper limits in Filament B of $n_e < 400$ cm$^{-3}$ in the pos1 and $n_e <$ 600 cm$^{-3}$ in the pos2. These low electron densities ($n_e < 400$ cm$^{-3}$) are consistent with other evolved SNRs, as shown in Fig. 5.

### 3.3 On the origin of the optical emission

G7.7–3.7 has been suggested to have its origin in the low-luminosity supernova SN 386 AD (Zhou et al. 2018). However, we did not detect a clear non-radiative Balmer shock emission which, with a few exceptions, pre-dominantly appears in younger SNRs (e.g. SN1006 and Tycho). This type of emission is also more common in SNRs

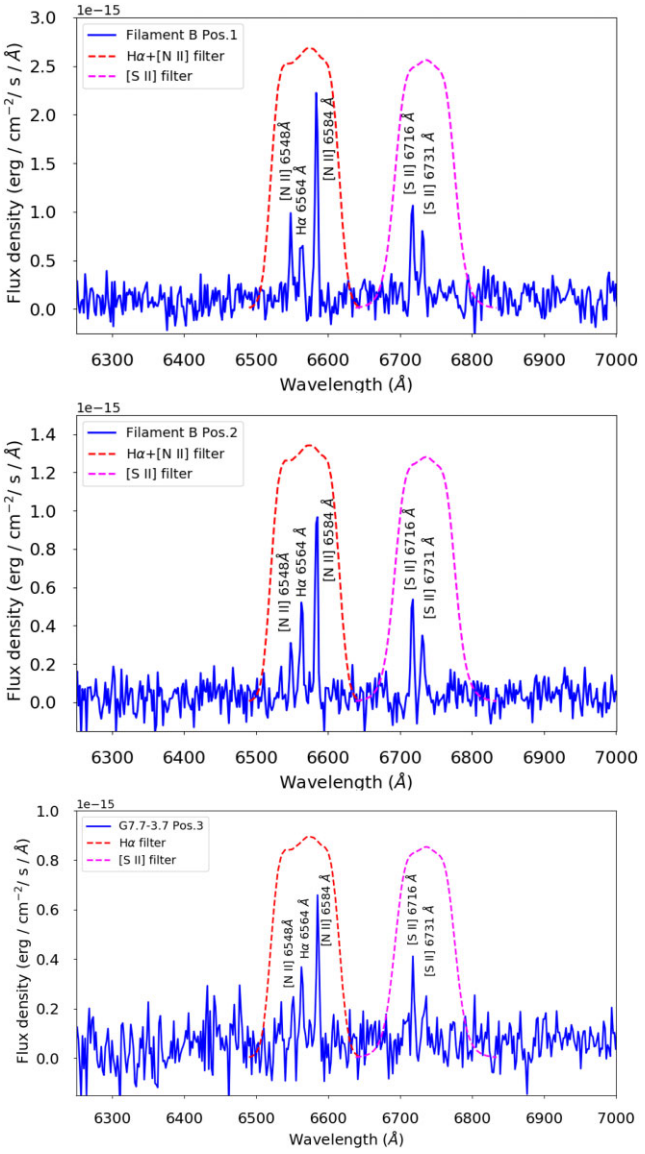


**Figure 4.** Long-slit low-resolution spectra for positions 1, 2, and 3 of Filament B (see Table 3) shown in the top, middle, and bottom panels, respectively. The WFC narrow filter band-passes (see Table 1) are also shown with dashed lines (red for the H $\alpha$ + [N II] and magenta for the [S II] filters).

**Table 3.** Relative line fluxes in different positions on Filament B. The errors of the emission line ratios are calculated through standard error propagation.

| | Pos.1 | | Pos.2 | | Pos.3 | |
|---|---|---|---|---|---|---|
| Line (Å) | $F^a$ | S/N[b] | $F$ | S/N | $F$ | S/N |
| [N II] 6548 | 130 | (6) | 56 | (3) | 54 | (2) |
| H $\alpha$ 6563 | 100 | (9) | 100 | (4) | 100 | (3) |
| [N II] 6584 | 310 | (18) | 159 | (9) | 150 | (6) |
| [S II] 6716 | 139 | (10) | 97 | (5) | 96 | (3) |
| [S II] 6731 | 112 | (8) | 85 | (4) | 66 | (2) |
| Absolute H $\alpha$ flux[c] | 4.1 ± 0.5 | | 3.4 ± 0.9 | | 2.1 ± 0.5 | |
| [S II]/H $\alpha$ | 2.51 ± 0.53 | | 1.83 ± 0.71 | | 1.63 ± 1.11 | |
| $F$(6716)/$F$(6731) | 1.24 ± 0.22 | | 1.14 ± 0.36 | | 1.45 ± 0.86 | |
| [N II]/H $\alpha$ | 4.40 ± 0.95 | | 2.15 ± 0.85 | | 2.04 ± 1.35 | |
| $n_e$[d] | <400 | | <600 | | – | |

[a]Observed fluxes normalized to $F$(H $\alpha$) = 100 and uncorrected for interstellar extinction. [b]Numbers in parentheses represent the signal-to-noise ratio of the quoted fluxes. [c]In units of $10^{-15}$ erg s$^{-1}$ cm$^{-2}$. [d]In units of cm$^{-3}$.

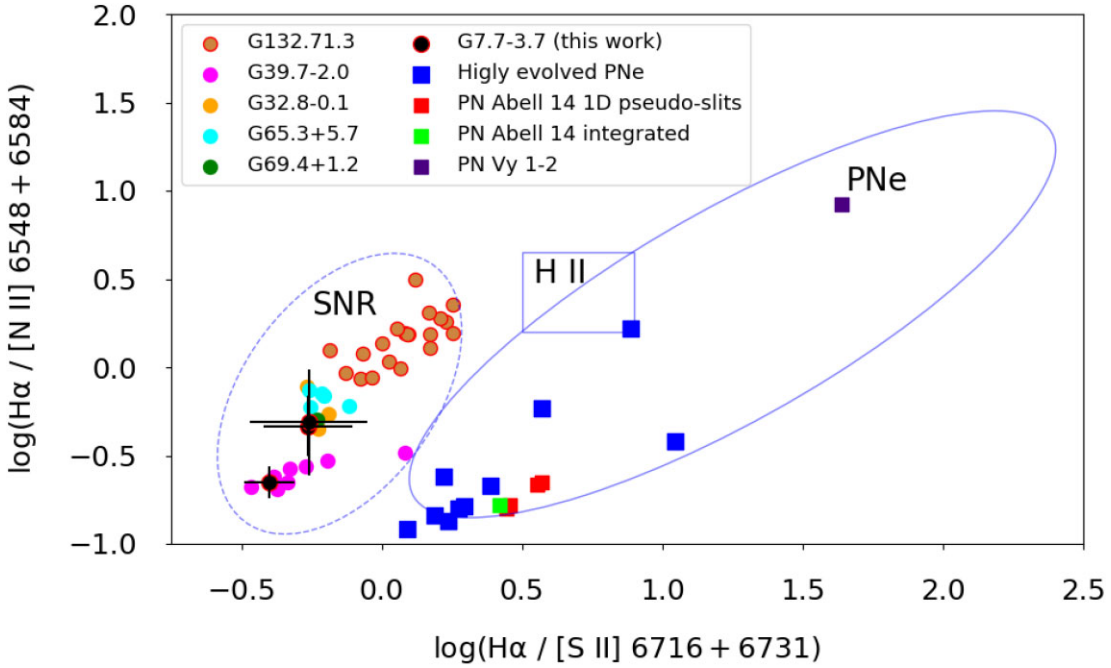


**Figure 5.** Emission line diagnostic diagram (Sabbadin et al. 1977) showing a number of SNRs (Boumis et al. 2022, 2009, 2007; Mavromatakis, Boumis & Paleologou 2002a; Mavromatakis et al. 2002b) and PNe (PN Vy 1-2 (Akras et al. 2015), highly evolved PNe (Akras et al. 2016), and PN Abell 14 (Akras et al. 2020) for comparison). The regimes of SNRs, PNe, and H II regions are also plotted. G7.7–3.7 (black circles) is well placed in the regime occupied by SNRs with low H $\alpha$/[S II] $\lambda\lambda$6716,6731 and H $\alpha$/[N II] $\lambda\lambda$6548,6584. The line ratios of G7.7–3.7 are taken from Table 3.

produced by Type Ia SNe, while G7.7–3.7 has been proposed to be a result of a low-luminosity Type IIP SN (Zhou et al. 2018). In addition, Balmer-dominated shocks are generally rather faint. Although strong Balmer shock emission can be excluded from the present data, there is still a possibility that some fainter emission remains undetected in the relatively crowded field.

The detected optical emission is consistent with radiative shocks, which can arise from SNRs that have evolved beyond the adiabatic phase, or by collision of the remnant's forward shock with a dense medium. To assess the plausibility of the first scenario, we estimate the transition radius ($R_{\rm PDS}$) between the Sedov and pressure-driven snowplow (PDS) phase, which marks the evolutionary moment that radiative shocks are expected to be formed (Cioffi, McKee & Bertschinger 1988):

$$R_{\rm PDS} = 14.0 \left(\frac{E}{10^{51}\ {\rm erg}}\right)^{\frac{2}{7}} \left(\frac{n_0}{{\rm cm}^{-3}}\right)^{-\frac{3}{7}} \zeta_{\rm m}^{-\frac{1}{7}}\ {\rm pc}, \quad (1)$$

where $E$ is the SN energy, $n_0$ is the ambient medium density, and $\zeta_{\rm m}$ is a constant equal to unity for solar metallicity. Adopting an ambient medium density in the range of $n_0 = 0.1$–$1\ {\rm cm}^{-3}$ (Zhou et al. 2018) and a typical SN energy of $E = 10^{51}$ erg the extracted radius is $R_{\rm PDS} = 14.0$–$37.5$ pc. For the case of a sub-energetic SN explosion of $E = 10^{50}$ erg, as suggested by Zhou et al. (2018), the corresponding radius is $R_{\rm PDS} = 7.3$–$19.5$ pc. Overall, the extracted transition radius range is larger than the observed radius of G7.7−3.7, being $R_{\rm s} \sim 12.8\, d_4$, where $d_4$ is the distance of the remnants in units of 4 kpc (Milne et al. 1986). This suggests that the remnant is still in the adiabatic phases of SNR evolution in which radiative shocks are not expected. The only exception is the case of a low-energy SN event embedded in a rather high-density ambient medium (e.g. for $E = 10^{50}$ erg and $n_0 = 1\ {\rm cm}^{-3}$ the transition radius is $R_{\rm PDS} = 7.3$ pc, smaller than the radius of G7.7–3.7). If indeed the remnant has entered the PDS phase then its age should be higher than the Sedov-PDS transition age ($t_{\rm PDS}$, Cioffi et al. 1988), i.e.

$$t_{\rm SNR} > t_{\rm PDS} = 1.33 \times 10^4 \left(\frac{E}{10^{51}\ {\rm erg}}\right)^{\frac{3}{14}} \left(\frac{n_0}{{\rm cm}^{-3}}\right)^{-\frac{4}{7}} \zeta_{\rm m}^{-\frac{5}{14}} = 8100\ {\rm yr}. \quad (2)$$

Such a scenario is inconsistent with the association of G7.7–3.7 with the SN 386 AD, as proposed by Zhou et al. (2018). However, if this is the case, then radiative shocks should be expected all over the periphery of the SNR – as most evolved SNRs display (e.g. Boumis et al. 2009; Fesen et al. 1995) – and not only to the south region of G7.7–3.7.

The problems discussed above can be resolved using an alternative explanation for the optical emission of G7.7–3.7, according to which the SNR blast is interacting with a dense shell in the southern region of the remnant. Hydrodynamic models of SNRs have shown that the collision of a shock wave with a dense region results in a substantial deceleration of the forward shock's velocity that – depending on the density contrast between the wall and the surrounding medium – can become almost instantaneously radiative (Dwarkadas 2005, 2007; Chiotellis, Schure & Vink 2012; Chiotellis et al. 2013). Within the framework of this scenario, the co-spatial X-ray emission of G7.7–3.7 can be attributed to the shocked gas that currently has collided with the high-density shell. Such a scenario has been studied in the context of the extended, young SNR RCW 86, the likely remnant of SN 185 (e.g. Broersen et al. 2014).

Regarding the formation mechanism of the density wall, the spatial locality of the optical emission and its proximity to the explosion centre indicates a circumstellar origin, associated with the mass outflow of the progenitor star. The presence of the density wall only at the south of the remnant could be attributed either to a non-spherical symmetric mass outflow from the parent star or/and to ISM density gradients in the form of random dense clouds that where lying close to the progenitor star and they have been mixed with

circumstellar material. A third alternative suggests that the progenitor was a supersonically moving, mass-losing star that formed a bow-shaped circumstellar structure around the explosion centre. Thus, the emission could be interpreted as the collision of the SNR blast wave with the portion of the bow-shaped circumstellar structure that is lying closest to the explosion centre (i.e. the region around the stagnation point). At the same time, the rest of the remnant still remains within the interior of the bubble being characterized by fast, non-radiative, X-ray emitting shocks.

### 3.4 Possible nitrogen overabundance?

The observed nitrogen enrichment of the shocked gas (see Table 3) advocates for the existence of circumstellar materials near the southern shell of the SNR. In the optical spectra of most older SNRs, the [N II] emission lines flanking H$\alpha$ emission have a lower flux than the H$\alpha$ emission. Fig. 4 shows that for G7.7–3.7 [N II]/6584 Å dominates over H$\alpha$. Only a few SNRs show this pattern, for example, radiative shocks in Kepler's SNR (Blair, Long & Vancura 1991, cf. knot D3 in their fig. 8), and one filament in Puppis A (Sutherland & Dopita 1995). The relatively high flux of [N II] is in those cases attributed to an enhanced nitrogen abundance, taken to be caused by pre-SN mass loss. The gas in the shell can also be a mixture of circumstellar and interstellar materials. The X-ray-emitting gas in the southern shell of G7.7–3.7 shows subsolar abundances from Oxygen to Iron (Zhou et al. 2018). Combined with the optical observation, this suggests that the pre-SN wind materials are rich in Nitrogen but not in heavier elements such as Oxygen.

Nitrogen-rich mass outflows in the form of stellar winds are expected by red supergiant (RSGs) progenitor stars (e.g. Origlia et al. 2016) or, in the low-mass regime, by stars in the asymptotic giant branch (AGB) with initial mass $\geq 4$ M$_\odot$ (e.g. Karakas et al. 2018). Nitrogen-rich Wolf−Rayet stars (Crowther 2007) is a third alternative but it is less likely as their stellar winds excavate very extended circumstellar structures due to their high wind mechanical luminosity (Smith 2014).

If indeed the SNR is evolving within the wind bubble of its progenitor star, we can provide a draft estimation of its age by employing the self-similar SNR evolution models of Chevalier (1982). In particular, describing the SN ejecta density with a power law of $\rho_{\rm ej} \propto r^{-n}$, with n = 7 and the wind-blown bubble in which the remnant is evolving with a density profile of $\rho_{\rm AM} = q\, r^{-s}$, where s = 2 and $q = \frac{\dot{M}_{\rm w}}{4\pi u_{\rm w}}$, with $\dot{M}_{\rm w}$ and $u_{\rm w}$, the stellar wind mass loss rate and terminal velocity respectively, the age of the remnant is given by

$$t_{\rm snr} = \left[\frac{R_{\rm s}}{1.3} \times \left(\frac{A\, g^n}{q}\right)^{\frac{1}{s-n}}\right]^{\frac{n-s}{n-3}}, \qquad (3)$$

where $A = 0.27$, $g = \left[\left(\frac{25}{21\pi}\right)\left(\frac{E_{\rm ej}^2}{M_{\rm ej}}\right)\right]^{\frac{1}{7}}$ with $E_{\rm ej}$ and $M_{\rm ej}$ the SN energy and ejecta mass, respectively and $R_{\rm s} = 12.8\, d_4$ pc, the current radius of the remnant. Adopting typical values for a Type II SN resulted by a red supergiant progenitor, namely $M_{\rm ej} = 6$–$9$ M$_\odot$, $E_{\rm ej} = 10^{51}$ erg, $\dot{M}_{\rm w} = 10^{-6}$–$10^{-5}$ M$_\odot$yr$^{-1}$, and $u_{\rm w} = 50$–$100$ km s$^{-1}$, we extract a range for the SNR age equal to $t_{\rm snr} = (1120$–$2610) d_4^{5/7}$ yr. For the case of a Type Ia progenitor, employing to equation (3) the relevant SN and AGB wind properties: $M_{\rm ej} = 1$–$1.4$ M$_\odot$, $E_{\rm ej} = 10^{51}$ erg, $\dot{M}_{\rm w} = 10^{-6}$–$10^{-5}$ M$_\odot$yr$^{-1}$, and $u_{\rm w} = 5$–$20$ km s$^{-1}$, the corresponding range of the SNR age is $t_{\rm snr} = (1070 - 2920) d_4^{5/7}$ yr. Both scenarios do not contradict to a possible association of G7.7–3.7 with the historical SN 386 AD as in such a case the current SNR age had to be $t_{\rm snr} = 1637$ yr. Thus, a possible association of G7.7–3.7 with SN 386 seems to be alighted to an evolutionary scenario according to which the remnant is evolving within the wind bubble formed by a Type II or Type Ia stellar progenitor and currently is partially colliding with a local circumstellar shell at the southern region of the SNR. Nevertheless, detailed hydrodynamic simulations are required to assess this statement.

## 4 CONCLUSIONS

We performed the first deep optical study in the direction of the SNR G7.7–3.7. The region of the SNR is mostly clear of diffuse optical emission. The only exception is in the south of the remnant, where the radio and X-ray emission has been previously detected. Here, we detected two filamentary structures clearly visible in the H$\alpha$ + [N II] filter, with fainter emission in the forbidden-line filters [O III] and [S II]. Both filaments – in particular Filament A – appear to correspond well with the location of the forward shock seen in X-rays.

Follow-up spectroscopic observations of one of the filaments revealed large ratios of [S II]/H$\alpha$ = (1.6–2.5), expected for SNR related shocks. In addition, the [S II] doublet ratio also suggests upper limits of electron density of the gas (<400 and <600 cm$^{-3}$, for positions 1 and 2 respectively; see Table 3 for more details). The emission line diagnostics suggest similar ratios as observed in other SNR, providing robust evidence against an H II region origin. Based on the filamentary morphology, spatial coincidence with the X-ray emission, and spectroscopic diagnostic line ratios that the optical emission discovered is associated to the SNR G7.7–3.7 originated by radiative shocks.

Our calculations show that the optical emission from the SNR is more likely to originate from the collision of forward shock with the locally higher density ISM. The SNR evolutionary phase could still be consistent with the radiative post-adiabatic phase, but this requires a subenergetic explosion ($E = 10^{50}$ erg) that occurred in an environment with $n_0 = 1$ cm$^{-3}$. This explanation would, however, put the age of the remnant closer to 8000 yr, which is inconsistent with the ionization age of the SNR as determined from X-ray observations. Such an inconsistency can be resolved if the optically emitting regions are associated with patches of gas with higher densities. Several young SNRs indeed show such radiative shocks like the historical SNR RCW 86 (SN 185), which is also a quite extended SNR, and Kepler's SNR (SN 1604), a more compact SNR. Moreover, the large ratio of [N II] over H$\alpha$ emission suggest that the gas is enriched in nitrogen, suggesting that the shock moves through material lost by the progenitor star. This is by itself an indication that G7.7–3.7 is a young or moderately aged SNR.

Our optical study does not allow to make a firm conclusion about whether G7.7–3.7 is indeed the remnant of the historical SN 386 AD. Despite the presence of radiative shocks, normally an indication of an older SNR, there are counter examples of young SNRs with radiative shocks, and the spectral/morphological properties of the optical emission from G7.7–3.7 matches these counter example. Given the interest in identifying new historical SNRs, our study suggest it is worthwhile to continue investigating G7.7–3.7 as the potential remnant of SN 386 AD.

## ACKNOWLEDGEMENTS

The work of VD is supported by a grant from NWO graduate programme/GRAPPA-PhD programme. VD also acknowledges support from the LKBF, subsidy no. 19.2.027. JVHS acknowledges

support from STFC grant ST/R000824/1. PZ acknowledges the support from the NWO Veni Fellowship, grant no. 639.041.647 and NSFC grant 11590781. SA thanks the support under the grant 5077 financed by IAASARS/NOA. AdB thanks the support from the Spanish Government Ministerio de Ciencia e Innovación through grants PGC-2018-091, 3741-B-C22, and SEV 2015-0548, from the Canarian Agency for Research, Innovation and Information Society (ACIISI) of the Canary Islands Government, and from the European Regional Development Fund (ERDF), under grant with reference ProID2017010115. We would like to acknowledge Jiang-Tao Li for the initial exploratory optical images of the field. VD and JVHS would also like to acknowledge the support of Leo Hernández-Suárez. AC gratefully acknowledges Mano Trampouli for the fruitful discussions and inspiration as well as the students of the 4rth Lykeion Acharnon for their support and motivation.

This research made use of ASTROPY, a community-developed core PYTHON package for Astronomy (Astropy Collaboration et al. 2013), MATPLOTLIB (Hunter et al. 2007), NUMPY (Harris et al. 2020), SCIPY (Virtanen et al. 2020), APLPY (Robitaille 2019), PANDAS (Pandas development team 2020), and LMFIT (Newville et al. 2014). We further made use of SAOIMAGE DS9 (Joye & Mandel 2003) and the SAO/NASA Astrophysics Data System. INT-WFC photometry was obtained as part of the ING.NL.19B.006 programme. The INT is operated on the island of La Palma by the Isaac Newton Group of Telescopes in the Spanish Observatorio del Roque de los Muchachos of the Instituto de Astrofísica de Canarias. The Pan-STARRS1 Surveys (PS1) and the PS1 public science archive have been made possible through contributions by the Institute for Astronomy, the University of Hawaii, the Pan-STARRS Project Office, the Max-Planck Society and its participating institutes, the Max Planck Institute for Astronomy, Heidelberg and the Max Planck Institute for Extraterrestrial Physics, Garching, The Johns Hopkins University, Durham University, the University of Edinburgh, the Queen's University Belfast, the Harvard-Smithsonian Center for Astrophysics, the Las Cumbres Observatory Global Telescope Network Incorporated, the National Central University of Taiwan, the Space Telescope Science Institute, the National Aeronautics and Space Administration under grant no. NNX08AR22G issued through the Planetary Science Division of the NASA Science Mission Directorate, the National Science Foundation grant no. AST-1238877, the University of Maryland, Eotvos Lorand University (ELTE), the Los Alamos National Laboratory, and the Gordon and Betty Moore Foundation. This work has made use of data from the European Space Agency (ESA) mission *Gaia* (https://www.cosmos.esa.int/gaia), processed by the *Gaia* Data Processing and Analysis Consortium (DPAC, https://www.cosmos.esa.int/web/gaia/dpac/consortium). Funding for the DPAC has been provided by national institutions, in particular the institutions participating in the *Gaia* Multilateral Agreement. We would also like to thank the anonymous referee for their comments that greatly improved this paper.

## DATA AVAILABILITY

The data underlying this article will be available at Zenodo repository after the completion of the referee process (https://doi.org/10.5281/zenodo.5121367).

## REFERENCES

Acero F. et al., 2016, ApJS, 224, 8
Akras S. et al., 2022, MNRAS, 512, 2202
Akras S., Boumis P., Meaburn J., Alikakos J., López J. A., Gonçalves D. R., 2015, MNRAS, 452, 2911
Akras S., Clyne N., Boumis P., Monteiro H., Gonçalves D. R., Redman M. P., Williams S., 2016, MNRAS, 457, 3409
Akras S., Monteiro H., Aleman I., Farias M. A. F., May D., Pereira C. B., 2020, MNRAS, 493, 2238
Arendt R. G., 1989, ApJS, 70, 181
Astropy Collaboration et al., 2013, A&A, 558, A33
Bertin E., Arnouts S., 1996, A&AS, 117, 393
Bilikova J., Williams R. N. M., Chu Y.-H., Gruendl R. A., Lundgren B. F., 2007, AJ, 134, 2308
Blair W. P., Long K. S., Vancura O., 1991, ApJ, 366, 484
Boumis P. et al., 2007, MNRAS, 381, 308
Boumis P. et al., 2022, MNRAS, 512, 1658
Boumis P., Xilouris E. M., Alikakos J., Christopoulou P. E., Mavromatakis F., Katsiyannis A. C., Goudis C. D., 2009, A&A, 499, 789
Broersen S., Chiotellis A., Vink J., Bamba A., 2014, MNRAS, 441, 3040
Castelli F., Kurucz R. L., 2003, in Piskunov N., Weiss W. W., Gray D. F., eds, Symposium - International Astronomical Union. Vol. 210, Cambridge University Press, Uppsala Sweden, p. A20, preprint( arXiv:astro-ph/0405087)
Chevalier R. A., 1982, ApJ, 258, 790
Chevalier R. A., Raymond J. C., Kirshner R. P., 1980, ApJ, 235, 186
Chiotellis A., Schure K. M., Vink J., 2012, A&A, 537, A139
Chiotellis A., Kosenko D., Schure K. M., Vink J., Kaastra J. S., 2013, MNRAS, 435, 1659
Cioffi D. F., McKee C. F., Bertschinger E., 1988, ApJ, 334, 252
Crowther P. A., 2007, ARA&A, 45, 177
Development Pandas , 2020, pandas-dev/pandas: Pandas, Zenodo, https://doi.org/10.5281/zenodo.3509134
Dubner G. M., Giacani E. B., Goss W. M., Moffett D. A., Holdaway M., 1996, AJ, 111, 1304
Dwarkadas V. V., 2005, ApJ, 630, 892
Dwarkadas V. V., 2007, ApJ, 667, 226
Erben T. et al., 2005, Astron. Nachr., 326, 432
Fesen R. A., Downes R. A., Wallace D., Normandeau M., 1995, AJ, 110, 2876
Flewelling H. A. et al., 2020, ApJS, 251, 7
Gaia Collaboration et al., 2016a, A&A, 595, A1
Gaia Collaboration et al., 2016b, A&A, 595, A2
Gaia Collaboration et al., 2023, A&A, 674, A1
Gardner F., Whiteoak J., Morris D., 1969, Australian J. of Phys., 22, 821
Ghavamian P., Raymond J., Hartigan P., Blair W. P., 2000, ApJ, 535, 266
Giacani E., Loiseau N., Smith M. J. S., Dubner G., Iacobelli M., 2010, in Comastri A., Angelini L.,Cappi M., eds, Proc. AIP Conf. Vol. 1248, Bologna Italy, p. 39. X-Ray Astronomy 2009; Present Status, Multi-Wavelength Approach and Future Perspectives.
Green D. A., 2015, MNRAS, 454, 1517
Harris C. R. et al., 2020, Nature, 585, 357
Heng K., 2010, PASA, 27, 23
Hester J. J., Raymond J. C., Blair W. P., 1994, ApJ, 420, 721
Hunter J. D., 2007, Comput. Sci. Eng., 9, 90
Joye W., Mandel E., 2003, in Payne H., Jedrzejewski R., Hook R., eds, ASP Conf. Ser. Vol. 295, Astronomical Data Analysis Software and Systems XII. Astron. Soc. Pac., San Francisco, p. 489
Kaplan D. L., Condon J. J., Arzoumanian Z., Cordes J. M., 1998, ApJS, 119, 75
Karakas A. I., Lugaro M., Carlos M., Cseh B., Kamath D., García-Hernández D. A., 2018, MNRAS, 477, 421
Leonidaki I., Boumis P., Zezas A., 2013, MNRAS, 429, 189
Long K. S., 2017, Handbook of Supernovae. Springer International Publishing, Cham, p. 2005, preprint (arXiv:1712.05331) , http://link.springer.com/10.1007/978-3-319-21846-5_90
Mavromatakis F., Boumis P., Paleologou E. V., 2002a, A&A, 387, 635
Mavromatakis F., Boumis P., Papamastorakis J., Ventura J., 2002b, A&A, 388, 355

Mccray R., 2017, Handbook of Supernovae. Springer International Publishing, Cham, p.2181 https://link.springer.com/10.1007/978-3-319-21846-5_96
Milisavljevic D., Fesen R. A., 2013, ApJ, 772, 134
Milne D. K., Roger R. S., Kesteven M. J., Haynes R. F., Wellington K. J., Stewart R. T., 1986, MNRAS, 223, 487
Milne D., Dickel J., 1974, Aust. J. Phys., 27, 549
Morlino G., Blasi P., Bandiera R., Amato E., Caprioli D., 2013, ApJ, 768, 148
Newville M., Stensitzki T., Allen D. B., Ingargiola A., 2014, LMFIT: Non-Linear Least-Square Minimization and Curve-Fitting for Python, Zenodo, https://doi.org/10.5281/zenodo.11813
Origlia L. et al., 2016, A&A, 585, A14
Parker Q. A. et al., 2005, MNRAS, 362, 689
Pastorello A. et al., 2004, MNRAS, 347, 74
Pavlovic M., Dobardzic A., Vukotic B., Urosevic D., 2014, Serb. Astron. J., 189, 25
Perek L., Kohoutek L., 1967, Catalogue of Galactic Planetary Nebulae. Publication House Czechoslovak Academy of Sciences, Prague
Ritter A., Parker Q. A., Lykou F., Zijlstra A. A., Guerrero M. A., Le Dû P., 2021, ApJ, 918, L33
Robitaille T., 2019, APLpy v2.0: The Astronomical Plotting Library in Python, Zenodo, https://doi.org/10.5281/zenodo.2567476
Sabbadin F., Minello S., Bianchini A., 1977, A&A, 60, 147
Samarakoon B., 2018, KDU J. Multidiscip. Stud. (KJMS), 1, 1
Sanduleak N., 1976, Publ. Warner & Swasey Obs., 2, 57
Schaefer B. E., 2023, MNRAS, 523, 3885
Schirmer M., 2013, ApJS, 209, 21
Smith N., 2014, ARA&A, 52, 487
Sutherland R. S., Dopita M. A., 1995, ApJ, 439, 365
Tody D., Society of Photo-Optical Instrumentation Engineers 1986, in Crawford D. L., ed., SPIE Conference Series Vol. 627, Instrumentation in Astronomy VI, Tucson United States, p. 733.
van den Bergh S., 1978, ApJS, 38, 119
Vink J., 2016, Handbook of Supernovae, Springer, Berlin, p.139
Vink J., 2020, Physics and Evolution of Supernova Remnants. Astronomy and Astrophysics Library. Springer International Publishing, Cham, http://link.springer.com/10.1007/978-3-030-55231-2
Vink J., Yamazaki R., 2013, ApJ, 780, 125

This paper has been typeset from a TEX/LATEX file prepared by the author.